Fully explicit formulae for flame speed in infinite and finite porous media

Pierre-Alexandre Masset, Omar Dounia, Laurent Selle

Fully-explicit formulae for flame speed in infinite and finite porous media

P.-A. Masset[a], O. Dounia[a] and L. Selle[a]

[a] Institut de Mécanique des Fluides, 2 allée du Professeur Camille Soula, 31400 Toulouse

ARTICLE HISTORY
Compiled September 1, 2020

ABSTRACT
A novel model for stationary flames in inert porous media is proposed. It is based on the hypothesis that interphase heat transfer has negligible impact on the local flame structure. This requires a gradual separation between the length scales of chemical reactions, gas diffusion, and interphase thermal re-equilibriation. It is shown that resolving the gas and solid equations without reaction on each side of the reaction sheet is sufficient to compute the preheating of the fresh gases ahead of the flame front. Combustion kinetics are solved separately, assuming the consumption rate to be a sole function of this preheating. Two kinetic models are considered, namely single-step Arrhenius and power law fits from experiments or detailed computations. Several fully-explicit formulae for flame speed in porous media are given accordingly. A universal abacus provides the maximum flame speed attainable in finite porous media. The explicit, ready-to-use nature of the present theory is particularly suitable for practical designs. This work is consistent with previous theoretical, numerical and experimental trends of the literature.

KEYWORDS
Porous media combustion, superadiabatic combustion, heat recirculation, porous design, flame speed porous media.

1. Introduction

Some key advantages of combustion in inert porous media are the increased flammability limits and stability, allowing a significant reduction in pollutant emissions (e.g. CO and NOx) [1–3]. The underlying mechanism is the preheating of the fresh gases, whose increased chemical reactivity allows to burn very lean mixtures [4–6]. This preheating is achieved by harvesting energy from the burnt gases through interphase heat exchange, which is then recirculated upstream by conduction and radiation in the porous matrix. Conceptually-speaking, the solid porous matrix is a supplementary path for upstream energy transfer to sustain combustion processes. Due to this preheating, the peak temperature in the gas domain may locally exceed the adiabatic temperature. This feature, characteristic of heat-recirculating burners, is often referred to as *superadiabatic* or *excess enthalpy* combustion.

Experimental investigations of flames submerged within porous media are intricate, mainly because of the opacity of the solid matrix and its small characteristic length scales. Measurements of temperature profiles, especially in the gas phase, are not trivial and may require advanced diagnostics [7, 8]. For example, to the authors' knowledge,

Corresponding author: P.-A. Masset / pierrealexandre.masset@imft.fr

a standard and essential quantity such as the local gas velocity has not been measured in these configurations. Regarding numerical simulations, there are many levels of approximation and corresponding modelling strategies. The most widespread may be the volume-averaged Navier-Stokes equations including reaction terms. This requires the determination of equivalent properties, such as a volume heat transfer coefficient, equivalent mixing diffusion or thermal conductivity, which may not be constant and cannot always be measured. The seminal works of Takeno et al. [9, 10] laid down the concept of excess enthalpy combustion, proposing numerical solutions in semi-infinite and finite geometries. Their one-dimensional model assumed constant solid temperature and single-step Arrhenius kinetics. Unlike classical gaseous combustion, mass flow rate and flame position were shown to be linked. A single branch was found in the semi-infinite case, while two branches were found in the finite case - meaning that for a given inlet velocity, two flame positions are possible. A critical mass flow rate defining blow-off was identified. A similar model was used by Yoshizawa et al. [11] to predict the temperature profile in the solid and the relative importance of diffusion, conduction, and reaction terms along the flow direction was discussed. Later, it was shown in [12] that the classical shortcomings of single-step kinetics were more limiting for configurations with strong heat recirculation, where slow chemical reactions may drive the global behavior. This motivated the extension of traditional, one-dimensional combustion codes such as Premix or Cantera to account for the inert porous matrix [13–16]. Albeit improving accuracy, general trends remain the same. Some authors also considered two-dimensional simulations, again with volume-averaged equations. Notably, the recent work of Li et al. [17] on a porous microcombustor may be highlighted for its careful choice of modelling constants. Given the importance of proper radiation modelling to enhance predictability, many authors also resolved the Radiative Transfer Equation or one of its various approximations [14, 16, 18–20]. At the other side of the numerical spectrum, Direct Pore Level Simulations (DPLS) were undertaken by some researchers, looking for insights on the corrugated flame structure intertwined in the porous structure [21, 22].

In parallel to numerical simulations, analytical works were carried out. By means of asymptotic theory, Dehaies and Joulin [23] studied the semi-infinite case of Takeno and Sato [9]. They also found one branch of solutions for inlet speed versus flame position. Buckmaster and Takeno [24] followed through to account for the finite case. They found two or more distinct branches, depending on flame position and heat losses to ambient. The apparition of a third or fourth branch stems from the consideration of *local* heat losses, leading to subadiabatic *weak flames*. Later on, Escobedo and Viljoen [25] were the first to propose an analytical approximation following a linearized Rosseland hypothesis. They discussed features of radiant efficiency and also found two distinct flame positions for a given inlet speed. Soon afterwards, Boshoff-Mostert and Viljoen [26] published an Arrhenius-based model which always led to superadiabatic temperatures, but their work did not catch the downstream branch found by most other authors. More recently, Pereira et al. [27–29] published a series of articles on the structure of a flame within infinite porous media. Unique feature of the literature, they treated in [28] the case of ultra-lean mixtures, where interphase heat exchange plays a role at the scale of gas diffusion. In the rest of the literature where interphase equilibrium is not assumed, authors considered diffusion and reaction zones to be exempt of interphase heat transfer. It means that apart from the matching conditions on each side of the reaction-diffusion region, the flame was often implicitly assumed to behave locally as an adiabatic free-flame.

It is worthwhile mentioning that the formalism of flames submerged within porous

media shares many traits with the study of combustion in micro and mesoscale tubes [30–36]. Conceptually, small tubes can be seen as a straightened porous structure also featuring substantial thermal coupling with the wall. Lee and Maruta [36] have described many stationary propagation regimes of the flame front through a theoretical one-dimensional, single-step Arrhenius model. They have shown that superadiabatic combustion with high wall temperatures occurs only for slowly-moving, almost stationary flames. This feature is coherent with the results of the vast literature on filtration combustion, where thermal and reaction waves should be superimposed to achieve maximum superadiabatic effect [37–42]. Unlike the present work, which considers stationary flames with substantial interphase non-equilibrium, filtration combustion focuses mainly on flame front propagation, assuming strong interphase equilibrium.

Despite the fact that many aspects of combustion in porous media have already been explored, it seems that a simple, fully-explicit formula for flame speed as a function of basic porous and mixture properties is yet to be proposed. For instance, the formula proposed by Pereira [27] requires to solve an implicit problem involving recirculation efficiency to obtain the flame speed. In addition, analytical models suffer from the single-step approximation, which may hide the actual sensitivity of the flame to preheating. Eventually, little practical design rules and universal relationships between infinite and finite porous media have been explored. The purpose of the present paper is to cover these issues, by proposing a novel and ready-to-use decoupled analytical model in both infinite and finite cases. Assuming the flame to behave locally as an adiabatic free-flame, it is be possible to 1) solve the thermal problem on each side of the reaction sheet so as to compute the preheating of the flame, and then 2) solve the chemical problem separately, so as to know how the flame responds to this preheating. The full modelling of each phase allows to predict when gas diffusion and interphase re-equilibriation length scales are well separated, assessing whether the local adiabaticity hypothesis is valid. Analytical approximations provide fully-explicit forms for the flame speed. The proposed decoupled methodology allows to consider complex chemistry through correlations of free-flames consumption rates as a function of preheating, thus offering alternatives to single-step. However, since the present model does not include local heat losses, it cannot account for weak-flame solutions. The present work is also meant to retrieve and discuss many key features of combustion within porous media from the literature, which can be summarised as follows:

- the flame structure consists of a macroscale preheating region, followed by a thin reaction-diffusion zone, then by another macroscale thermal relaxation region (counterpart of the preheating region, of comparable length) ;
- recirculation efficiency decreases with equivalence ratio and porosity, and increases with solid conductivity and volume heat transfer coefficient ;
- for finite porous media, two or more solutions may be found for a given inlet speed.

The paper is organised as follows. Section 2 treats the case of the infinite porous medium, and several fully-analytical expressions for flame speed-up are provided. Section 3 is dedicated to the influence of finite length on flame stabilization and recirculation efficiency.

2. Infinite porous medium

2.1. Configuration

The configuration sketched in Figure 1 represents a steady flame submerged in an infinite, inert and homogeneous porous medium, characterised by its porosity ϵ, thermal conductivity λ_s, and surface density $\mathcal{S}_V$. The problem is assumed to be one-dimensional along the space coordinate x, and the steady flame is localized at the arbitrary position $x = 0$ by its reaction zone, assumed infinitely thin. The gas phase is characterised by

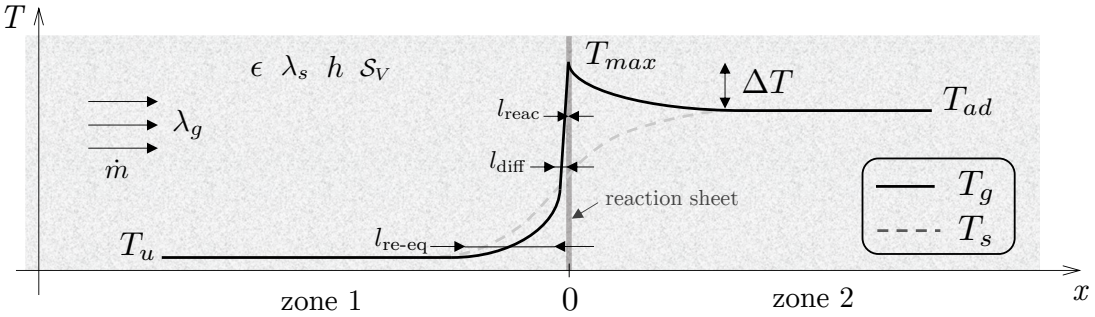

Figure 1.: Principle: flame submerged within infinite porous medium.

its thermal conductivity λ_g and heat capacity per mass unit c_{p_g}. The temperature of the solid and gas phases are denoted T_s and T_g, respectively and the heat flux between the two phases is modelled via a classical transfer coefficient h. A mass flow rate per surface unit $\dot{m}$ of premixed gas is imposed upstream at a temperature T_u. The system is assumed to be globally adiabatic so that far downstream both solid and gas temperatures equal the adiabatic equilibrium temperature T_{ad}. Due to the presence of the solid matrix, the gas is preheated before reaching the flame front. This may lead to a maximum gas temperature T_{max} above the adiabatic temperature, which will be shown in Appendix B to be reached at the origin in the reaction zone. This classical behavior of combustion in inert porous media is quantified via the so-called excess temperature ΔT, defined as:

$$\Delta T = T_{max} - T_{ad}. \tag{1}$$

If the reactive-diffusive flame structure is not affected by interphase heat transfer, then ΔT is also the preheating temperature perceived upstream the flame front. We now discuss this hypothesis, and see how it corresponds to what we call the *decoupled* methodology.

2.2. Modelling assumptions and decoupled methodology

An adiabatic free-flame front may be divided into two regions [43]:

- a non-reactive, diffusion zone of length l_{diff}, where the heat from the reaction zone is diffused upstream through a steep temperature gradient ;
- a reactive zone of length l_{reac} where the chemical energy of the mixture is released. Classically, one finds $l_{\text{reac}} \ll l_{\text{diff}}$.

For flames embedded in porous media, a third length scale $l_{\text{re-eq}}$ intervenes, related to the interphase re-equilibrium zones on each side of the flame front, as shown in

Figure 1. Under the assumption of length scale separation, that is:

$$l_{\text{re-eq}} \gg l_{\text{diff}} \gg l_{\text{reac}}, \tag{2}$$

the flame in the porous medium can be considered *locally adiabatic* and interphase heat exchange plays a minor role at the scale of diffusion and reaction. This hypothesis, corresponding to (2) is adopted in the present work. It notably allows for decoupling the analysis into two distinct, independent problems:

- a thermal problem $\mathcal{T}$, which provides the preheating temperature ΔT as a function of the inlet mass flux $\dot{m}$. It is obtained by solving the non-reactive, coupled gas and solid equations on each side of the reaction sheet;
- a chemical problem $\mathcal{C}$, which describes the sensitivity the consumption rate $\dot{m}$ to the preheating ΔT.

Formally, these two problems can be written:

$$\Delta T = \mathcal{T}(\dot{m}) \qquad \text{and} \qquad \dot{m} = \mathcal{C}(\Delta T). \tag{3}$$

Combining them leads to an implicit formulation:

$$\dot{m} = (\mathcal{C} \circ \mathcal{T})(\dot{m}), \tag{4}$$

whose resolution provides the value of $\dot{m}$ consistent with both the non-reactive equations outside the reaction sheet and the local sensitivity of the flame to preheating. The benefits of the methodology are the following. Solving the non-reactive equations boils down to simple linear algebra. Under the some hypotheses, notably Equation (2), the preheating/excess temperature finds a simplified expression. Also, both single-step and more complex chemistry can be considered for the resolution of Equation (4).

2.3. Thermal problem $\mathcal{T}$

In this section, the thermal problem $\mathcal{T}$ is solved both numerically and analytically.

2.3.1. Equations and boundary conditions

On each side of the flame, no reaction occurs. Consequently, the steady-state, isobaric, volume averaged one-dimensional energy equations for the solid and gas phase read [44]:

$$\lambda_s \, \partial_x^2 T_s + \frac{h_V}{1-\epsilon}(T_g - T_s) = 0 \qquad \text{(solid)}, \tag{5}$$

$$-\dot{m} c_{p_g} \, \partial_x T_g + \lambda_g \, \partial_x^2 T_g - \frac{h_V}{\epsilon}(T_g - T_s) = 0 \qquad \text{(gas)}, \tag{6}$$

where $h_V = h \, \mathcal{S}_V$ is the heat exchange coefficient per unit volume. The porous medium is assumed globally adiabatic, thus there are no heat losses in the equations. This justifies the boundary conditions for the gas and solid phases, which must reach thermal

equilibrium far upstream and downstream:

$$T_s \xrightarrow[x\to-\infty]{} T_u \quad \text{and} \quad T_g \xrightarrow[x\to-\infty]{} T_u, \tag{7}$$

$$T_s \xrightarrow[x\to+\infty]{} T_{ad} \quad \text{and} \quad T_g \xrightarrow[x\to+\infty]{} T_{ad}. \tag{8}$$

2.3.2. Dimensionless equations

The coordinates and temperatures are normalized as:

$$x^* = x/\sqrt{\frac{(1-\epsilon)\lambda_s}{h_V}}, \quad \theta_s = \frac{T_s - T_u}{T_{ad} - T_u}, \quad \theta_g = \frac{T_g - T_u}{T_{ad} - T_u} \quad \text{and} \quad \theta_{max} = \frac{T_{max} - T_u}{T_{ad} - T_u}. \tag{9}$$

It follows that the reduced adiabatic temperature is, by definition: $\theta_{ad} = 1$. Also, since $T_{ad} - T_u$ represents the thermal load, it is found that the dimensionless preheating temperature ΔT identifies to the recirculation efficiency:

$$\eta_{rec} = \frac{\Delta T}{T_{ad} - T_u} = \frac{T_{max} - T_u}{T_{ad} - T_{ad}} = \theta_{max} - \theta_{ad} = \theta_{max} - 1. \tag{10}$$

For a given mixture, the knowledge of η_{rec} is thus directly equivalent to that of ΔT:

$$\Delta T = \alpha\, T_{ad}\, \eta_{rec}, \tag{11}$$

where $\alpha = (T_{ad} - T_u)/T_{ad}$. Equations (5-6) can be normalised using (9), yielding:

$$\partial^2\theta_s + \theta_g - \theta_s = 0, \tag{12}$$

$$-r_{\dot{m}}\, \partial\theta_g + r_\lambda\, \partial^2\theta_g + \theta_s - \theta_g = 0, \tag{13}$$

where $\partial \equiv \partial_{x^*}$ and:

$$r_{\dot{m}} = \frac{\dot{m}\,\epsilon\, c_{p_g}}{\sqrt{h_V(1-\epsilon)\lambda_s}} \qquad \text{and} \qquad r_\lambda = \frac{\epsilon\,\lambda_g}{(1-\epsilon)\lambda_s}. \tag{14}$$

The product $h_V(1-\epsilon)\lambda_s$ can be interpreted as a conductance for the recirculated heat, first harvested via h_V, then conducted upstream through the solid matrix via $(1-\epsilon)\lambda_s$. As such, the quantity $r_{\dot{m}}$ can be seen as a ratio between the thermal load, proportional to $\dot{m}c_{p_g}$, and the energy recirculated upstream by the solid. Thus, the inverse of $r_{\dot{m}}$ is expected to be closely related to the recirculation efficiency. The other ratio, r_λ, represents the ability of the system to conduct energy, either in the gas with the term $\epsilon\,\lambda_g$, or through the solid with the term $(1-\epsilon)\lambda_s$. The solutions for the solid and gas temperatures are respectively noted θ_s^1, θ_g^1 in zone 1, and θ_s^2, θ_g^2 in zone 2. Following Equations (7-8), the normalised boundary conditions are:

$$\theta_s^1 \xrightarrow[x^*\to-\infty]{} 0 \quad \text{and} \quad \theta_g^1 \xrightarrow[x^*\to-\infty]{} 0 \tag{15}$$

$$\theta_s^2 \xrightarrow[x^*\to+\infty]{} 1 \quad \text{and} \quad \theta_g^2 \xrightarrow[x^*\to+\infty]{} 1 \tag{16}$$

Combining Equations (12-13), the problem reduces to a single linear differential equation for θ_s with constant coefficients, valid in both zones:

$$\partial \left[r_\lambda \, \partial^3 - r_{\dot{m}} \, \partial^2 - (r_\lambda + 1) \, \partial + r_{\dot{m}} \right] \theta_s = 0. \tag{17}$$

By integrating Equation (17) once and applying the boundary conditions (15-16), the governing equation in each zone becomes:

$$\left[r_\lambda \, \partial^3 - r_{\dot{m}} \, \partial^2 - (r_\lambda + 1) \, \partial + r_{\dot{m}} \right] \theta_s^1 = 0 \quad \text{in zone 1,} \tag{18}$$

$$\left[r_\lambda \, \partial^3 - r_{\dot{m}} \, \partial^2 - (r_\lambda + 1) \, \partial + r_{\dot{m}} \right] (\theta_s^2 - 1) = 0 \quad \text{in zone 2.} \tag{19}$$

The general solutions of Equations (18-19) are linear combinations of exponentials, whose eigenvalues are given by the roots of the same characteristic polynomial:

$$r_\lambda \, \lambda^3 - r_{\dot{m}} \, \lambda^2 - (r_\lambda + 1) \, \lambda + r_{\dot{m}} = 0. \tag{20}$$

For $\dot{m} > 0$, the roots are necessarily two positive reals and a negative one, ordered $\lambda_1 < 0 < \lambda_2 < \lambda_3$. A proof and further details are provided in Appendix C. Since the boundary conditions require boundedness at $x \to \pm\infty$, the solutions of Equations (18) and (19) for the solid temperature take the following form:

$$\theta_s^1(x^*) = A_2 e^{\lambda_2 x^*} + A_3 e^{\lambda_3 x^*}, \tag{21}$$

$$\theta_s^2(x^*) = 1 + A_1 e^{\lambda_1 x^*}. \tag{22}$$

Using Equation (12), the gas temperature is also found:

$$\theta_g^1(x^*) = A_2(1 - \lambda_2^2) e^{\lambda_2 x^*} + A_3(1 - \lambda_3^2) e^{\lambda_3 x^*}, \tag{23}$$

$$\theta_g^2(x^*) = 1 + A_1(1 - \lambda_1^2) e^{\lambda_1 x^*}. \tag{24}$$

The determination of the three unknowns A_1, A_2 and A_3 requires three jump conditions between zones 1 and 2, at $x = 0$. Assuming negligible interphase heat exchange at the scale of the reaction zone, the temperature of the solid and its derivative are necessarily continuous across the flame:

$$T_s(x = 0^-) = T_s(x = 0^+), \tag{25}$$

$$\partial_x T_s(x = 0^-) = \partial_x T_s(x = 0^+). \tag{26}$$

For the gas, the conservation of enthalpy across the flame reads:

$$\lambda_g \, \partial_x T_g(x = 0^-) = \dot{m} c_{p_g} (T_{ad} - T_u) + \lambda_g \, \partial_x T_g(x = 0^+). \tag{27}$$

It is shown in Appendix A that Equation (27), together with Equation (26) and the boundary conditions (15-16) is in fact equivalent to imposing gas temperature continuity.The three jump conditions are thus:

$$\theta_s^1(x^* = 0^-) = \theta_s^2(x^* = 0^+) \qquad \text{continuity of solid temperature,} \tag{28}$$

$$\partial\theta_s^1(x^* = 0^-) = \partial\theta_s^2(x^* = 0^+) \qquad \text{continuity of solid heat flux,} \tag{29}$$

$$\theta_g^1(x^* = 0^-) = \theta_g^2(x^* = 0^+) \qquad \text{continuity of gas temperature.} \tag{30}$$

Applying the boundary conditions (28-30) to Equations (21-22), one gets a linear system:

$$A_2 + A_3 - A_1 = 1, \tag{31}$$

$$\lambda_2 A_2 + \lambda_3 A_3 - \lambda_1 A_1 = 0, \tag{32}$$

$$A_2(1-\lambda_2^2) + A_3(1-\lambda_3^2) - A_1(1-\lambda_1^2) = 1, \tag{33}$$

whose resolution gives the coefficients A_i, thus the temperature profiles. The formal solution is provided in Appendix B. As explained in Section 2.1, the temperature of interest is the maximum temperature found at the origin:

$$\theta_{max} = \theta_g^1(x^* = 0^-) = \theta_g^2(x^* = 0^+). \tag{34}$$

Using Equations (10) and (24) yields:

$$\eta_{rec} = \theta_g^2(x^* = 0^+) - 1 = A_1(1-\lambda_1^2), \tag{35}$$

proving that heat recirculation depends only on the smallest (negative) solution of Equation (20), which depends *a priori* on both $r_{\dot{m}}$ and r_λ. Formally, using (10) the solution of the thermal problem $\mathcal{T}$ writes:

$$\Delta T = (T_{ad} - T_u)\ \eta_{rec}(r_{\dot{m}}, r_\lambda). \tag{36}$$

2.3.3. Numerical solutions of the thermal problem

Before providing an analytical solution for η_{rec}, let us take a look at particular solutions to gain physical insight on the model and the range of validity of its underlying assumptions. Examples of temperature profiles are shown in Figure 2 for four different inlet mass fluxes and given porous/mixture properties, i.e. four different values of $r_{\dot{m}}$ for a given value of r_λ. It is observed that the solid temperature does not exceed the adiabatic temperature, which is coherent with most findings in the literature. A graphical representation of the recirculation efficiency η_{rec}, as defined in Equation (35), is shown in Figure 2(a). Looking at the temperature increase in the gas by diffusion, near to the origin, in Figures 2(a) and 2(b), it is very sharp and a clear distinction between the lengths scales of preheating and gas diffusion is observed. However, on Figures 2(c) and 2(d), $\theta_s \sim \theta_g$ except in the vicinity of the flame because of the much stronger interphase equilibrium. These two solutions for small mass fluxes are therefore not valid, first because the hypothesis of local adiabaticity in the flame front seems to be violated and second because given the high preheating ($\theta_g > 0.9$ before the flame front) auto-ignition is likely to occur. Examination of the four cases presented in Figure 2 suggests that there are lower bounds for both $r_{\dot{m}}$ and $r_{\dot{m}}/r_\lambda$ below which the solution may not be valid. This is attributed to the violation of the scale-separation hypothesis (2). Using this preliminary observation, a necessary condition for the validity of the model is proposed:

$$r_{\dot{m}} \gg 0.1 \qquad \text{and} \qquad r_{\dot{m}}/r_\lambda \gg 10. \tag{37}$$

In order to investigate these limitations in a more systematic way, the numerical solutions of η_{rec} are plotted versus $r_{\dot{m}}$ for different values of r_λ in Figure 3. The four

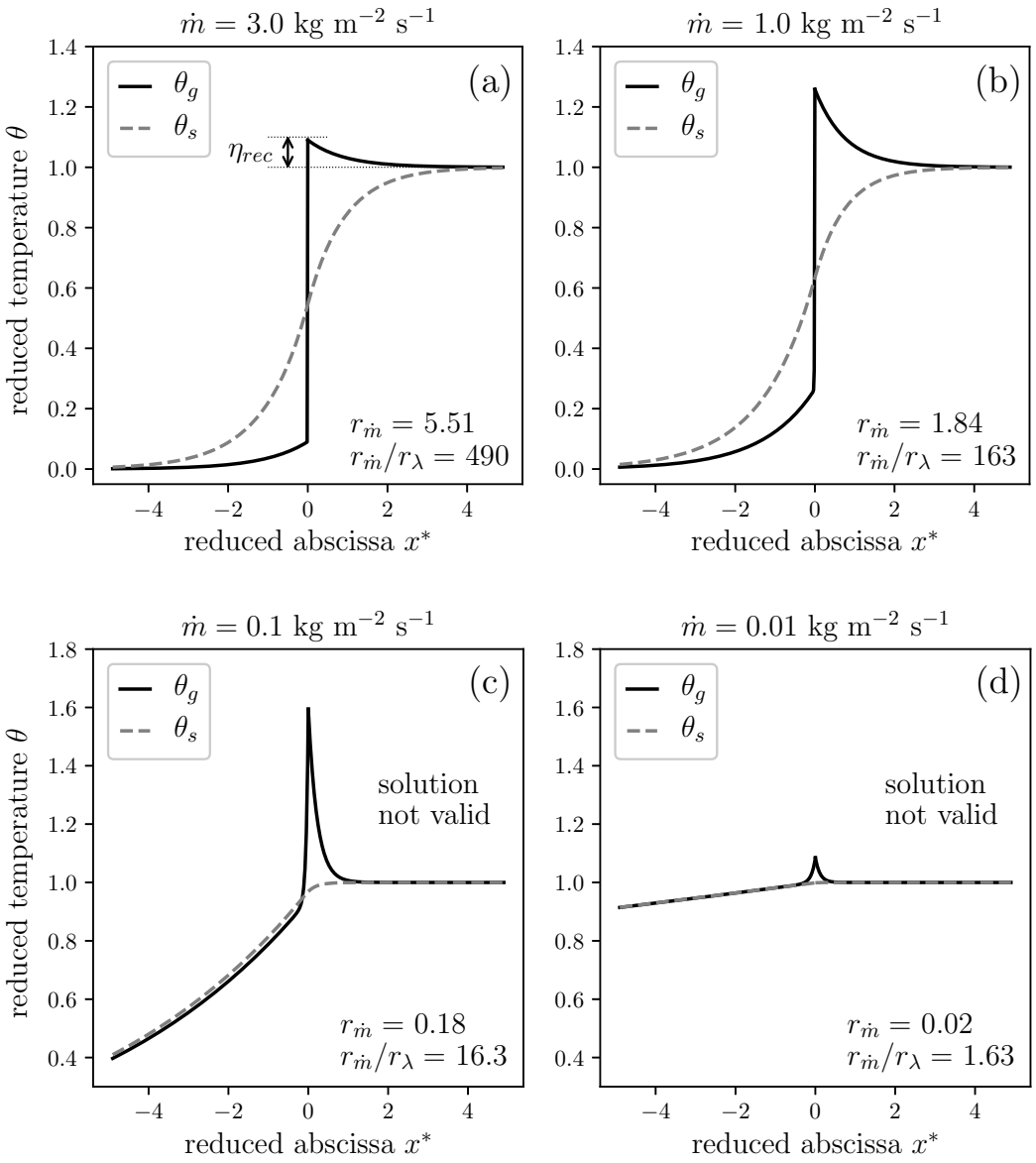

Figure 2.: Temperature profiles for four different inlet mass flow rates and $r_\lambda = 0.01$. The parameters used are: $\epsilon = 0.8$, $\lambda_s = 20$ W m^{-1} K^{-1}, $\lambda_g = 0.025$ W m^{-1} K^{-1}, $h_V = 1.2 \times 10^5$ W m^{-3} K^{-1}, and $c_{p_g} = 10^3$ J kg^{-1} K.

cases of Figure 2 are also displayed. Typical values representative of combustion in porous media can be found in [27], where $r_{\dot{m}} = 1.78$ and $r_\lambda = 0.07$. By covering two orders of magnitude above and below these values, the proposed range should cover most porous media and mixtures. The solutions verifying $r_{\dot{m}} > 0.5$ and $r_{\dot{m}}/r_\lambda > 50$, consistent with assumptions (37), are drawn in solid lines, while the others are drawn in dotted lines. Interestingly, these solid lines seem to collapse the dashed curve whose equation is $1/2r_{\dot{m}}$, with little influence of the parameter r_λ. In summary, it seems that under the assumptions (37):

- the lengths scales of preheating and gas diffusion are well separated (*cf.* Figure 2),

which is consistent with the modelling assumptions;
- the solution of the thermal problem can be approximated by $\eta_{rec} \simeq 1/2r_{\dot{m}}$.

Similar ranges were explored in previous studies. For example, the case $r_\lambda \ll 1$ was considered by Lee and Maruta for mesoscale tubes [36]. The limits considered by Pereira [27] were 1) $r_\lambda \ll 1$ if $\epsilon/(1-\epsilon) = O(1)$ and 2) $r_{\dot{m}}^2/r_\lambda \gg 1$ if $\epsilon = O(1)$. By combining $r_{\dot{m}} \gg 0.1$ and $r_{\dot{m}}/r_\lambda \gg 10$, this latter limit is retrieved, without the influence of porosity which is not considered in [27] to discriminate asymptotic regimes.

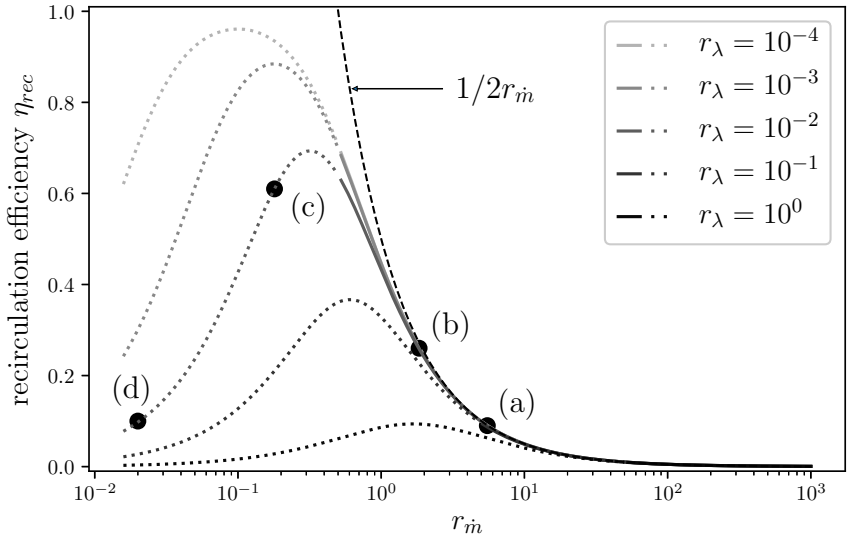

Figure 3.: Recirculation efficiency η_{rec} for various values of the dimensionless parameters $r_{\dot{m}}$ and r_λ. Solid lines: $r_{\dot{m}} > 0.5$ and $r_{\dot{m}}/r_\lambda > 50$. Dotted lines: $r_{\dot{m}} < 0.5$ or $r_{\dot{m}}/r_\lambda < 50$. The points (a-d) correspond to Figure 2.

2.4. Length scales separation and approximation of η_{rec}

2.4.1. Length scales separation

In this Section, mathematical developments and physical interpretation are provided under the assumption (37). First, let us recall that since $\sqrt{(1-\epsilon)\lambda_s/h_V}$ is the length used to normalize the equations, each root λ_i of (20) found in the exponentials of Equations (23-24) provides a dimensional length scale l_i given by:

$$l_i = \frac{\sqrt{(1-\epsilon)\lambda_s/h_V}}{|\lambda_i|}. \tag{38}$$

It is thus of interest to find the expression of the roots λ_i in the regime (37). Their rigorous, general forms and Taylor expansions in the regime (37) are given in Appendix C.

At the leading order, it is found that:

$$\lambda_1 \simeq -1, \qquad \lambda_2 \simeq 1 \qquad \text{and} \qquad \lambda_3 \simeq \frac{r_{\dot{m}}}{r_\lambda}, \tag{39}$$

so that:

$$l_1 \simeq l_2 \simeq \sqrt{\frac{(1-\epsilon)\lambda_s}{h_V}} \qquad \text{and} \qquad l_3 \simeq \frac{\lambda_g}{\dot{m}\, c_{p_g}}. \tag{40}$$

l_3 is the well-known gas diffusion length scale, denoted l_{diff}, while l_1 and l_2 define the typical length of interphase thermal re-equilibriation, denoted $l_{\text{re-eq}}$:

$$l_{\text{re-eq}} = \sqrt{\frac{(1-\epsilon)\lambda_s}{h_V}}. \tag{41}$$

This scale characterises the preheating and interphase relaxation regions before and after the flame front, as can be seen on Figures 2(a) and (b). This analysis gives an interpretation of $r_{\dot{m}}/r_\lambda$ as a ratio of length scales:

$$\frac{r_{\dot{m}}}{r_\lambda} = \sqrt{\frac{(1-\epsilon)\lambda_s}{h_V}} \Big/ \left(\frac{\lambda_g}{\dot{m} c_{p_g}}\right) = \frac{l_{\text{re-eq}}}{l_{\text{diff}}}. \tag{42}$$

The condition $r_{\dot{m}}/r_\lambda \gg 10$ is thus consistent with the separation of length scales of Equation (2) underlying the decoupled hypothesis of the present modelling.

2.4.2. Approximation of η_{rec}

Combining Equations (B3) and (C7-C9) into Equation (35), the leading-order analytical solution for the heat recirculation is:

$$\eta_{rec} \simeq \frac{1}{2r_{\dot{m}}}, \tag{43}$$

which is exactly the asymptote plotted in Figure 3. In this regime, the thermal problem does not depend on r_λ, which is coherent with the collapse of the curves in Figure 3. Equation (43) supports further the discussion of Section 2.3.2 on the physical significance of $r_{\dot{m}}$ and that of Section 2.3.3 on the condition $r_{\dot{m}} \gg 0.1$, showing that the approximate solution is valid when heat recirculation is not overly intense. In dimensional terms, the solution for $\mathcal{T}$ in Equation (3) is therefore:

$$\Delta T = (T_{ad} - T_u)\frac{\sqrt{h_V(1-\epsilon)\lambda_s}}{2\,\dot{m}\,\epsilon\, c_{p_g}}. \tag{44}$$

It is insightful to understand which physical properties are likely to play a signiticant part in validating the regime (37) or not. These are:

- the mass flow rate $\dot{m}$: very slow flames might show a strong interphase equilibrium. This regime was studied thoroughly by Pereira et al. [28];

- the solid thermal conductivity λ_s: its decrease leads to a lower separation of length scales. Its value will vary a lot with regard to the tortuosity of the porous matrix. Reticulated foams with little struts might have a much lower value than the original thermal conductivity of the material;
- the volume heat transfer coefficient h_V is also a key parameter which is often difficult to assess [1]. It is typically affected by the material surface state, the geometry, the Reynolds number, etc.

2.5. Chemical problem - model closure

In the present section, two paths for the resolution of the chemical problem $\mathcal{C}$ are proposed. Each time, the principle is to find a kinetic relation between the inlet mass flux $\dot{m}$ and the preheating of the fresh gases ΔT. First, a single-step Arrhenius estimation based on the work of Pereira et al. [27] is investigated. Then, a power law approximation of the consumption rate increase with preheating is identified through numerical simulations of adiabatic free-flames. For the sake of the example, two typical mixtures are considered: one methane-air and one hydrogen-air, whose descriptive values are given in Table 1. The parameter β is the so-called Zel'dovich number, related to the

mixture	$\boldsymbol{\phi}$	$\boldsymbol{\alpha}$	$\boldsymbol{\beta}$	$\boldsymbol{T_{ad}}$ **(K)**
methane-air	0.80	0.85	9.07	1996
hydrogen-air	0.52	0.82	8.27	1683

Table 1.: Relevant thermodynamic and chemical properties for two reacting mixtures used as examples.

activation temperature T_a through:

$$\beta = \frac{T_a(T_{ad} - T_u)}{T_{ad}^2}. \tag{45}$$

Values for β in Table 1 are found in [27] for methane and [45] for hydrogen. In what follows, S_L^P denotes the global consumption speed (*i.e.* the gas velocity at the infinite upstream), and $S_L^0(T)$ the speed of the corresponding adiabatic free-flame of fresh gases at a temperature T. The flame speed-up is defined as the ratio $S_L^P/S_L^0(T_u)$. It quantifies the acceleration of combustion due to the heat recirculation in the porous matrix. This speed-up is also that of the mass fluxes and is directly related to $\dot{m}$, thus $\mathcal{C}(\Delta T)$, through:

$$\frac{S_L^P}{S_L^0(T_u)} = \frac{\dot{m}}{\dot{m}_0} = \frac{\mathcal{C}(\Delta T)}{\dot{m}_0}. \tag{46}$$

where $\dot{m}_0 = \rho_u \, S_L^0(T_u)$ is the mass flux of the adiabatic free-flame without porous medium and ρ_u is the density at the infinite upstream. Note that $\dot{m}_0$ is an input of the model in the sense that ρ_u and $S_L^0(T_u)$ are known *a priori*.

2.5.1. Single-step kinetics

The first kinetic model is based on the theoretical work of Peireira et al. [27]. They analyzed the asymptotic structure of a flame submerged in a porous medium. Alike

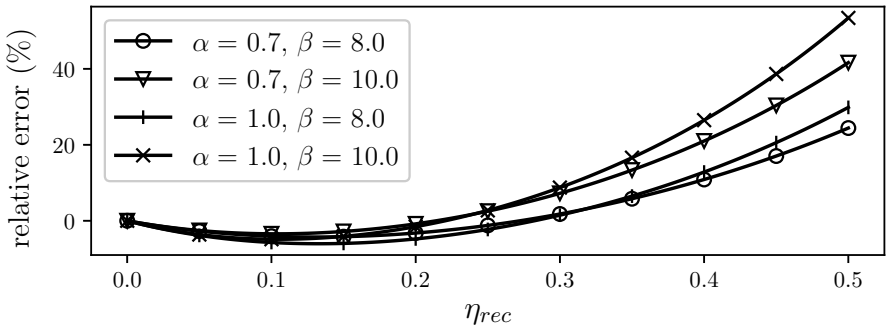

Figure 4.: Relative error between Equations (47) and (48).

the present model, their methodology consisted in neglecting interphase heat exchange at the scale of reaction and diffusion. They made use of a single-step Arrhenius law, and matched the preheating and flame exit gas temperature gradients - something not caught by the present model, but of negligible importance in the regime (2). For a null temperature exponent in the Arrhenius term, they found the following expression for flame speed-up:

$$\frac{S_L^P}{S_L^0(T_u)} = (1 + \alpha\eta_{rec}) \exp\left(\frac{1}{2}\frac{\beta\eta_{rec}}{1 + \alpha\eta_{rec}}\right). \tag{47}$$

In coherence with the regime (37), assuming $\alpha\eta_{rec}$ small enough yields a simplified expression for Equation (47):

$$\frac{S_L^P}{S_L^0(T_u)} = \exp\left(\frac{\beta\eta_{rec}}{2}\right). \tag{48}$$

The relative error between Equations (47) and (48) is plotted in Figure 4 for representative values of α and β. This shows that (48) is a fair approximation of (47) only for recirculation efficiencies below 0.3. Using this simplification, the derivation is pursued and we define:

$$\eta_{rec}^0 = \eta_{rec}\frac{\dot{m}}{\dot{m}_0}, \tag{49}$$

which, using Equation (43), yields:

$$\eta_{rec}^0 = \frac{\sqrt{h_V(1-\epsilon)\lambda_s}}{2\,\dot{m}_0\,\epsilon\,c_{p_g}}. \tag{50}$$

This shows that η_{rec}^0 is a constant related to the physical properties of the mixture and the porous medium. Then using Equations (46) and (49), Equation (48) becomes:

$$Z = W \exp(W), \tag{51}$$

where:

$$Z = \frac{\beta \eta_{rec}^0}{2} \qquad \text{and} \qquad W = \frac{\beta \eta_{rec}^0}{2} \frac{\dot{m}_0}{\dot{m}}. \tag{52}$$

The solution of Equation (51) is given by the the first branch of the Lambert function $\mathcal{W}$ [46]. Recalling Equation (46), this yields a fully-explicit formula for flame speed-up:

$$\frac{S_L^P}{S_L^0(T_u)} = \frac{\beta \eta_{rec}^0}{2\,\mathcal{W}(\beta \eta_{rec}^0/2)} \tag{53}$$

In order to discuss trends, Equation (53) is further simplified in the limit of small η_{rec}^0 using the Taylor expansion of $\mathcal{W}(Z)$ at the origin:

$$\mathcal{W}(Z) = Z - Z^2 + O(Z^3), \tag{54}$$

which simplifies Equation (53) to:

$$\frac{S_L^P}{S_L^0(T_u)} \simeq 1 + \frac{\beta}{2} \eta_{rec}^0. \tag{55}$$

2.5.2. Power law approximation

In this study, it is assumed (*cf.* (2)) that preheating and combustion are decoupled meaning that the local flame velocity is that of a preheated laminar adiabatic flat flame, *i.e.* $S_L^0(T_u + \Delta T)$. Mass conservation in steady state reads:

$$\rho(T_u) S_L^P = \rho(T_u + \Delta T) S_L^0(T_u + \Delta T), \tag{56}$$

which in the case of small pressure drop yields:

$$\frac{S_L^P}{S_L^0(T_u)} = \left(\frac{T_u}{T_u + \Delta T} \right) \frac{S_L^0(T_u + \Delta T)}{S_L^0(T_u)}. \tag{57}$$

Consequently, the determination of the flame speed-up only requires the knowledge of the adiabatic flame speed S_L^0 at T_u and $T_u + \Delta T$. Within a given temperature range it is common practice to fit experimental or numerical results via a power law. In order to simplify the algebra, one can choose a power of $(1 + \Delta T/T_u)$ in which case equation (57) reduces to:

$$\frac{S_L^P}{S_L^0(T_u)} = \left(1 + \frac{\Delta T}{T_u} \right)^{n_T} = \left(1 + \frac{T_{ad}}{T_u}\, \alpha\, \eta_{rec} \right)^{n_T}. \tag{58}$$

Examples corresponding to the two mixtures of Table 1 are shown in Figure 5, where the reference flame speeds have been computed with Cantera [47] using GriMech 3.0. In both cases, the power law approximation is quite accurate. Note that since overly large preheating temperatures lead to auto-ignition and a lack of numerical convergence of the adiabatic flames, the maximal preheating temperature is set to 300 K, which leads to different bounds in terms of η_{rec} between the two plots.

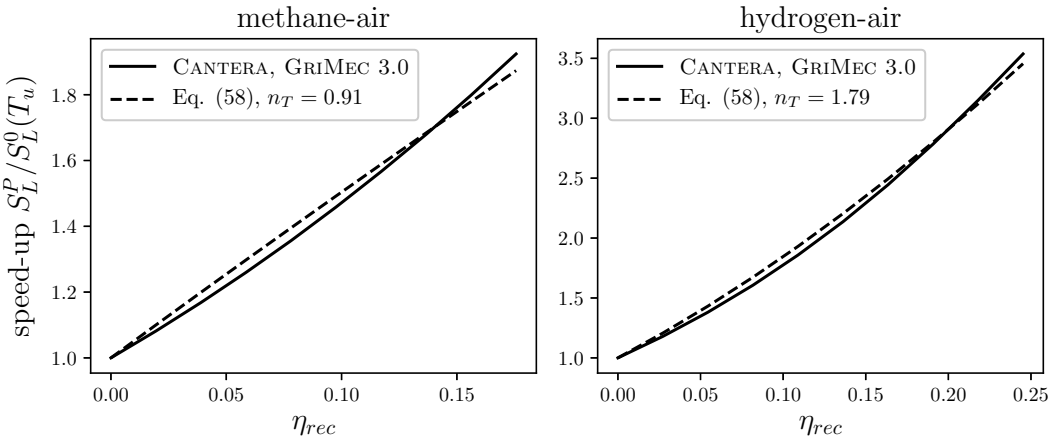

Figure 5.: Speed-up of the porous medium system: numerical simulations and power law correlations.

Following this approximation, an analytical formulation for the chemical problem is obtained by feeding Equations (46) and (49) into (58):

$$\left(\frac{S_L^P}{S_L^0(T_u)}\right)^{\frac{1}{n_T}+1} - \frac{S_L^P}{S_L^0(T_u)} = \frac{T_{ad}}{T_u}\,\alpha\,\eta_{rec}^0. \tag{59}$$

Because this equation is not amenable to a general analytical solution, two special cases are considered. First in the limit of small η_{rec}^0, a first-order Taylor expansion yields:

$$\frac{S_L^P}{S_L^0(T_u)} \simeq 1 + n_T\,\frac{T_{ad}}{T_u}\,\alpha\,\eta_{rec}^0. \tag{60}$$

Then in the special case $n_T = 1$:

$$\frac{S_L^P}{S_L^0(T_u)} = \frac{1}{2}\left[1 + \sqrt{1 + 4\,\frac{T_{ad}}{T_u}\,\alpha\,\eta_{rec}^0}\right]. \tag{61}$$

2.6. Discussion and validation

Several fully-explicit formulae for flame speed-up were derived in Section 2.5: Equation (55) for single-step Arrhenius; Equations (60) and (61) assuming a power-law sensitivity to temperature for the adiabatic free-flame speed. Both Equations (55) and (60) are first-order approximations where the speed-up is proportional to η_{rec}^0, with a slope depending on the sensitivity of their respective chemical model. These are useful to analyse general trends of flames with heat recirculation. As already discussed in the literature: recirculation efficiency decreases with porosity, and increases with solid conductivity and volume heat transfer coefficient. In addition, it is found here that recirculation efficiency increases with the adiabatic temperature T_{ad} and decreases with the fresh gases temperature T_u and adiabatic free-flame speed. Fur-

thermore, the previously-observed decrease in recirculation efficiency with equivalence ratio can be explained as resulting from the larger impact of equivalence ratio on $\dot{m}_0$ than T_{ad}. Equations (53) and (59) are more general solutions of the chemical problem but because they respectively require the knowledge of the Lambert function and a numerical integration, they are less useful for interpretation.

These analytical solutions are now compared to a numerical resolution using the software CANTERA with the GRIMECH 3.0 chemical scheme. For this validation, CANTERA was coupled to an in-house code solving the thermal problem in the solid matrix. The initial condition is set using the present analytical derivations and the two solvers are coupled until convergence. The two mixtures of Table 1 are considered with the following properties for the porous: $\epsilon = 0.9$, $\lambda_s = 10\ \mathrm{W\,m^{-1}\,K^{-1}}$, and $h_V = 1 \times 10^4\ \mathrm{W\,m^{-3}\,K^{-1}}$. This leads to the values $r_{\dot{m}} = 5.29$, $r_{\dot{m}}/r_\lambda = 70.5$ for the methane-air mixture and $r_{\dot{m}} = 8.06$, $r_{\dot{m}}/r_\lambda = 109.7$ for hydrogen-air, all falling within the regime (37). As expected, Equations (53) and (59) are more accurate than their

	CANTERA	**(53)**	**(55)**	**(59)**	**(60)**	**(61)**
methane-air	1.64	1.59	1.74	1.54	1.85	1.59
hydrogen-air	1.48	1.43	1.51	1.68	2.02	1.40

Table 2.: Validation of the speed-up $\boldsymbol{S_L^P/S_L^0(T_u)}$: comparison between a reference numerical simulation with CANTERA and GRIMECH 3.0 and the various formulae derived in this work.

corresponding first-order approximation, namely Equations (55) and (60). Thanks to its non-linear behavior, Equation (61) is quite close to the reference simulation, albeit assuming $n_T = 1$.

As a concluding remark, it is important to stress the implications of the choice of β *a priori*. Equations (55) and (60) show that speed-up is given, at the first-order, by η_{rec}^0 times a certain coefficient expressing the chemical sensitivity of the mixture to preheating. It is $\beta/2$ for single-step and $\alpha\, T_{ad}/T_u\, n_T$ for power law. Classically, hydrogen-air mixtures have lower activation energies compared to methane-air mixtures, as can be seen in Table 1. This apparently contradicts the fact that n_T is larger for hydrogen-air, as shown in Figure 5. This arises from the fact that β is usually fitted for a given global behavior (such as auto-ignition delay, laminar flame speed, or flame thickness) at given temperature and pressure. Note that, for a fixed activation temperature, β decreases when increasing inlet temperature. Therefore, single-step models using a fixed β do not account *a priori* for the variation of flame speed with preheating. A better strategy could consist in fitting a single value for activation temperature for various temperatures of fresh gases and applying an iterative procedure for the value of β as a function of η_{rec}, which technically varies for the equivalent local free-flame.

3. Effects of finite length

In this section, we investigate the role of finite length on superadiabatic properties and recirculation efficiency. The influence of radiant heat losses at the extremities of the porous is also studied. It is shown that the maximum recirculation efficiency in a porous of finite length converges towards that of its infinite counterpart in a universal manner.

3.1. Problem formulation

A flame submerged in a finite porous medium is now considered such as depicted in Figure 6. In addition to the parameters defined in Section 2, both the length of the porous medium L and the distance of the reaction sheet from the inlet $x_p \in [0, L]$ are specified. For the flame to be submerged, only porous much longer than the diffusion length scale are considered:

$$L \gg l_{\text{diff}}. \tag{62}$$

Using (41) and (42), this condition becomes:

$$L^* \gg \frac{r_\lambda}{r_{\dot{m}}}. \tag{63}$$

Four regions are distinguished: G1 and G2 are the gaseous zones before and after the porous medium, while S1 and S2 are the two-phase zones before and after the reaction sheet. The porous inlet is located at $x = -x_p$ and the outlet at $x = L - x_p$. Heat losses via radiation are noted J_{left} at the inlet and J_{right} at the outlet. All corresponding dimensionless quantities are noted with the * superscript.

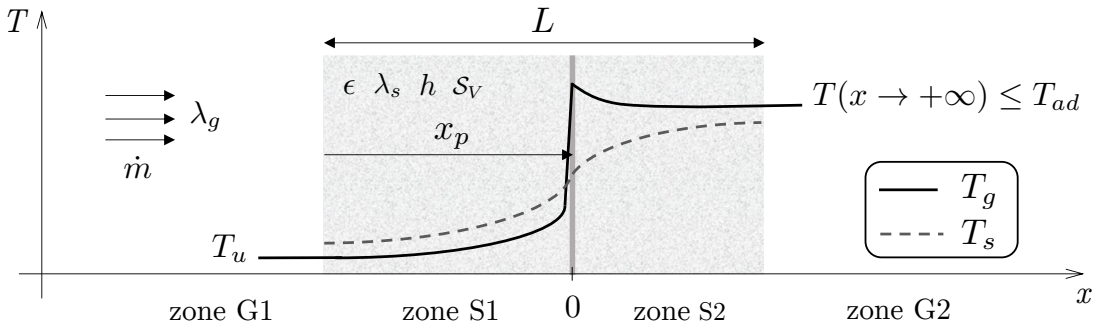

Figure 6.: Principle: flame submerged in a finite porous medium.

Alike the infinite case, the principle here is to find the flame speed-up in function of an implicit formulation (4), but this time, there is one distinct problem for each prescribed flame position x_p. Since this position changes the temperature profiles, thus heat recirculation, the flame speed-up is expected to be a function of x_p. One can anticipate that when the flame is close to the inlet or the outlet heat exchange with the solid is limited, thus reducing the speed-up. A maximum speed-up is therefore expected for a flame around the mid-section of the porous medium. The objectives of this Section are to predict the speed-up for a given flame position and quantify the influence of the finite porous length.

For zones S1 and S2, the governing equations remain that of the infinite case (5-6), whose general solutions are:

$$\theta_s^{S1}(x^*) = A_0^{S1} + \sum_{i=1}^{3} A_i^{S1} e^{\lambda_i x^*} \qquad \text{and} \qquad \theta_s^{S2}(x^*) = A_0^{S2} + \sum_{i=1}^{3} A_i^{S2} e^{\lambda_i x^*}. \tag{64}$$

Again, λ_i are the roots of the polynomial (20) for which $\lambda_1 < 0 < \lambda_2 < \lambda_3$. This time, the two constants A_0^{S1} and A_0^{S2} must be determined using the conditions all over the

domain, not just the boundary conditions. For the zones G1 and G2, the modelling reduces to a single gas equation without coupling with the solid:

$$-\dot{m} c_{p_g} \, \partial_x T_g + \lambda_g \, \partial_x^2 T_g = 0. \tag{65}$$

Normalisation yields:

$$\partial \left[-r_{\dot{m}} \, \theta_g + r_\lambda \, \partial \theta_g \right] = 0, \tag{66}$$

whose solutions compatible with the boundary conditions are respectively:

$$\theta_g^{G1}(x^*) = A_0^{G1} e^{\frac{r_{\dot{m}}}{r_\lambda} x^*} \qquad \text{and} \qquad \theta_g^{G2}(x^*) = A_0^{G2}. \tag{67}$$

In zone G2, the temperature $\theta_g^{G2}(x^*)$ is a constant, whose value is determined by the gas temperature continuity at the exit of the solid. It is as such an output of the problem, not an unknown:

$$A_0^{S2} = \theta_g^{G2}(x^*) = \theta_g^{S2}(x^* = L^* - x_p^*). \tag{68}$$

This leaves 9 unknowns for 9 jump conditions: the A_i^{S1}, the A_i^{S2} and A_0^{G1} are to be determined. At the flame front, we have:

$$\theta_s^{G1}(x^* = 0^-) = \theta_s^{G2}(x^* = 0^+) \qquad \text{continuity of solid temperature,} \tag{69}$$

$$\partial\theta_s^{G1}(x^* = 0^-) = \partial\theta_s^{G2}(x^* = 0^+) \qquad \text{continuity of solid heat flux,} \tag{70}$$

$$\theta_s^{G1}(x^* = 0^-) = \theta_s^{G2}(x^* = 0^+) \qquad \text{continuity of gas temperature,} \tag{71}$$

$$\partial\theta_g^{G1}(x^* = 0^-) = \frac{r_{\dot{m}}}{r_\lambda} + \partial\theta_g^{G2}(x^* = 0^+) \qquad \text{continuity of gas heat flux.} \tag{72}$$

This time, both gas continuity and the energy release from reaction must be prescribed. This is due to the indirect relation of the constants A_0^{S1} and A_0^{S2} to the boundary conditions at the infinite. Then, at the porous inlet, possible radiant heat losses must be accounted for, as well as the effect of porosity on gas heat flux continuity:

$$\partial\theta_s^{G1}(x^* = -x_p^*) = J_{\text{left}}^* \qquad \text{inlet radiant heat loss,} \tag{73}$$

$$\partial\theta_g^{G1}(x^* = -x_p^*) = \epsilon \, \partial\theta_g^{S1}(x^* = -x_p^*) \qquad \text{continuity of gas heat flux,} \tag{74}$$

$$\theta_g^{G1}(x^* = -x_p^*) = \theta_g^{S1}(x^* = -x_p^*) \qquad \text{continuity of gas temperature.} \tag{75}$$

At the outlet, the gas temperature gradient must go to zero because the gas temperature in region G2 is constant, so that:

$$\partial\theta_s^{G2}(x^* = L^* - x_p^*) = -J_{\text{right}}^* \qquad \text{outlet radiant heat loss,} \tag{76}$$

$$\partial\theta_g^{G2}(x^* = L^* - x_p^*) = 0 \qquad \text{continuity of gas heat flux.} \tag{77}$$

In the adiabatic case, it is trivial that $J_{\text{left}}^* = 0$ and $J_{\text{right}}^* = 0$. When considering

radiant heat losses using a Stephan model, it is found that:

$$J^*_{\text{left}} = \sqrt{\frac{1-\epsilon}{h_V \lambda_s}}\,\sigma\, T_u^4 \left(1 + \alpha \frac{T_{ad}}{T_u}\theta_s^{S1}(x^* = -x_p^*)\right)^4, \tag{78}$$

$$J^*_{\text{right}} = \sqrt{\frac{1-\epsilon}{h_V \lambda_s}}\,\sigma\, T_u^4 \left(1 + \alpha \frac{T_{ad}}{T_u}\theta_s^{S2}(x^* = L^* - x_p^*)\right)^4. \tag{79}$$

The jump conditions (69-77) can be recast under matrix formalism as:

$$\underline{\underline{\mathbf{M}}} \cdot \boldsymbol{A} = \boldsymbol{B}, \tag{80}$$

where $\boldsymbol{A}$ is the column matrix of unknowns:

$$\boldsymbol{A} = \left[A_0^{S1} \;\; A_1^{S1} \;\; A_2^{S1} \;\; A_3^{S1} \;\; A_0^{S2} \;\; A_1^{S2} \;\; A_2^{S2} \;\; A_3^{S2} e^{\lambda_3 (L^* - x_p^*)} \;\; A_0^{G1} e^{-\frac{r_{\dot{m}}}{r_\lambda} x_p^*}\right]^T, \tag{81}$$

and $\boldsymbol{B}$ the second member:

$$\boldsymbol{B} = \left[0 \;\; 0 \;\; 0 \;\; r_{\dot{m}}/r_\lambda \;\; J^*_{\text{left}} \;\; 0 \;\; 0 \;\; -J^*_{\text{right}} \;\; 0\right]^T. \tag{82}$$

The matrix $\underline{\underline{\mathbf{M}}}$ is provided in Appendix D. Note that in Equation (81), the coefficient A_3^{S2} is lumped together with $e^{\lambda_3 (L^* - x_p^*)}$ and A_0^{G1} with $e^{-\frac{r_{\dot{m}}}{r_\lambda} x_p^*}$. This allows for a well-conditioned numerical inversion of Equation (80). A close look at Equations (82) and (D1) reveals that η_{rec} depends this time on more than $r_{\dot{m}}$ and r_λ. In the adiabatic case, the solution is a function of L and x_p, but also of ϵ through the inlet jump condition (74). This latter dependency is very small for flames several gas diffusion length scales away from the porous inlet. This motivated some authors to discard the influence of porosity at the inlet and use directly a Dirichlet condition instead. When considering radiant heat losses, the non-linearity of J^*_{left} and J^*_{right} brings supplementary dependencies, namely of T_{ad}, T_u and the parameter $\sqrt{(1-\epsilon)/h_V\lambda_s}$. Numerically, this non-linearity is treated using a basic recursive method.

Examples of gas and solid temperature profiles are shown in Figure 7, without and with radiant heat losses, together with that of the same infinite porous. As expected, the reduction of the preheating length leads to a lower superadiabaticity compared to the infinite case. Since interphase non-equilibrium (*i.e.* $\theta_g - \theta_s$) is higher, the preheating rate is also higher and the preheating temperature gradient steeper. Regarding radiant heat losses, one can see in Figure 7 that they lead to a reduction in both gas and solid temperature at the outlet of the porous.

3.2. Influence of flame position

As anticipated, finite porous lengths reduce heat recirculation and therefore superadiabaticity. For a more detailed analysis of this effect, Figure 8 presents the recirculation efficiency η_{rec} versus the reduced flame position x_p^* for various reduced porous lengths L^*, at a given arbitrary inlet mass flux. It is observed that the maximum superadiabatic effect in the porous increases with porous length until $L^* \sim 5$. In these situations, the effects of finite length are not perceivable for a flame deep inside the porous. In parallel, it is observed that radiant heat losses lead to lower recirculation efficiencies. Overall, Figure 8 indicates that recirculation efficiency is a concave, direct function of

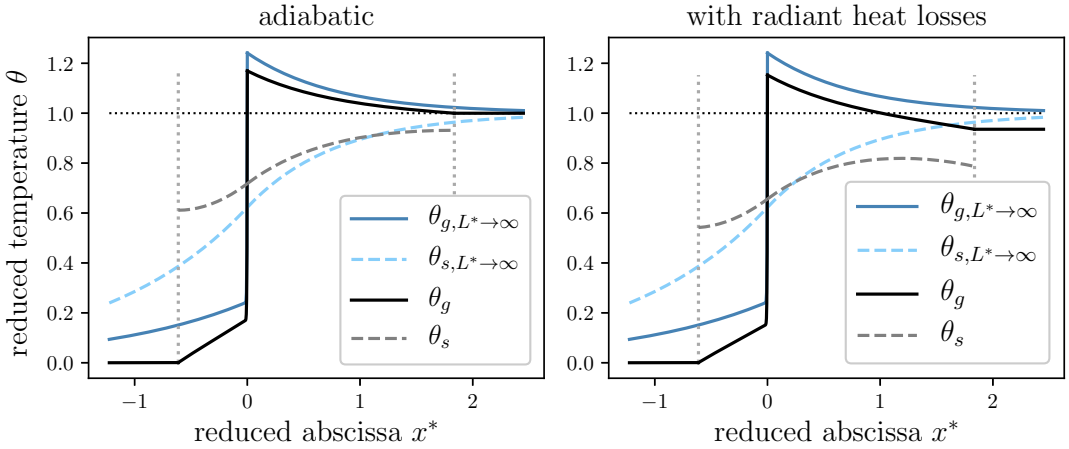

Figure 7.: Example of temperature profiles: adiabatic and radiant heat losses cases. The solution of the equivalent infinite porous is superimposed for comparison. The parameters used are: $T_u = 300$ K, $T_{ad} = 2000$ K, $\epsilon = 0.8$, $\lambda_s = 20$ W m^{-1} K^{-1}, $\lambda_g = 0.025$ W m^{-1} K^{-1}, $h_V = 6 \times 10^4$ W m^{-3} K^{-1}, $c_{p_g} = 10 \times 10^3$ J kg^{-1} K, $L = 2$ cm, $\dot{m} = 1.2$ kg m^{-2} s^{-1}, and $x_p = L/4$.

flame position. And since speed-up is a monotonous function of η_{rec}, a similar trend is expected for the flame speed-up. This is indeed observed in Figure 9, where $S_L^P/S_L^0(T_u)$ is plotted versus flame position x_p^*. It appears that the flame speed is also a function of flame position, with an upstream and a downstream branch: for a given inlet mass flux, two solutions are possible, on each side of the porous. Following the rationale of other authors, notably that of Diamantis [19], only the upstream branch is expected to be stable. A graphical explanation for the stability is that close to the inlet, the speed-up increases if the flame is pushed back while near the outlet, the speed-up decreases with x^*.

3.3. Universal behavior of finite-length effects in the decoupled regime

As discussed above, Figures 8 and 9 show a convergence of the maximum superadiabaticy, typically when $L^* > 5$. We now investigate the universality in this convergence. Figure 10 shows ratios of the maximum recirculation efficiency obtained in a finite porous medium $\eta_{rec}^{max}(L^*)$ and the one found in its infinite counterpart $\eta_{rec}(\infty)$, for various values of $r_{\dot{m}}$, r_λ and L^*. The chosen values satisfy the decoupled regime (37) and submerged flame (63) conditions. All these cases are very close to the limit case $r_{\dot{m}} \to \infty$, $r_\lambda \to 0$ with relative differences below 5%. For the sake of clarity, only a few cases are presented in Figure 10 but they cover all the solid line regions of Figure 3. This is a strong indication that finite-length effects only depend on the normalised length L^* and confirms that for $L^* > 5$, a porous matrix can be treated as infinite from the perspective of heat recirculation.

This is arguably of great practical interest. Using the model presented in Section 2 (either numerical integration or analytical approximations), one can compute $\eta_{rec}(\infty)$. Then with Figure 10, one can estimate finite-length effects and obtain the numerical value for $\eta_{rec}^{max}(L^*)$. This means that heat recirculation and flame speed-up can be anticipated at the design stage of a porous burner using intrinsic properties of the

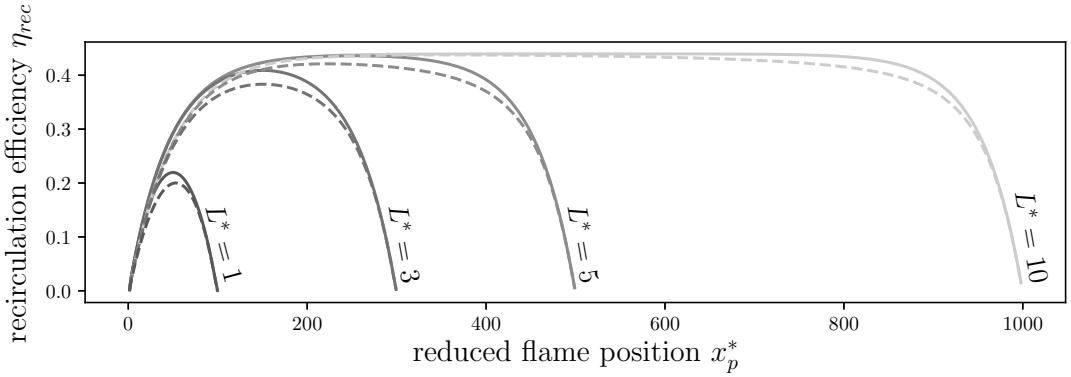

Figure 8.: Recirculation efficiency versus flame position for various lengths of porous media. Solid line: adiabatic case. Dashed line: with radiant heat losses. Parameters used: $T_u = 300$ K, $T_{ad} = 2000$ K, $\epsilon = 0.8$ and $\sqrt{(1-\epsilon)/h_V \lambda_s} = 2 \times 10^{-4}$ m^2 K W^{-1} for the radiant heat losses case.

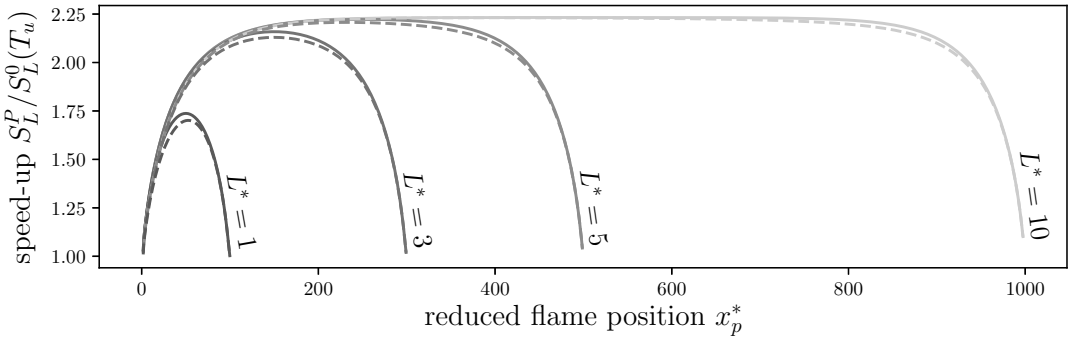

Figure 9.: Speed-up ratio versus flame position for various lengths of porous media. Solid line: adiabatic case. Dashed line: with radiant heat losses. The parameters used are: $T_u = 300$ K, $T_{ad} = 2000$ K, $\epsilon = 0.8$, $\lambda_s = 20$ W m^{-1} K^{-1}, $\lambda_g = 0.025$ W m^{-1} K^{-1}, $h_V = 2.4 \times 10^5$ W m^{-3} K^{-1}, $c_{p_g} = 10 \times 10^3$ J kg^{-1} K, $\dot{m}_0 = 1.2$ kg m^{-2} s^{-1}, and $n_T = 1$.

gaseous and solid phases. In other words, it is possible to use the speed-up formulae proposed in the infinite case, by multiplying η_{rec}^0 by the value of the ratio reported from Figure 10.

4. Conclusion

In this work, a one-dimensional framework is considered for the modelling of combustion in porous media. Heat losses are neglected in the sense that the domain is globally adiabatic and the case of an infinite porous media is considered first. Under the assumption of scale-separation for interphase heat exchange, gas diffusion and combustion, several analytical, fully explicit formulae were derived for the heat recirculation efficiency and flame acceleration. Major trends were spelled out, namely: a decrease with equivalence ratio, porosity and ambient temperature, and an increase

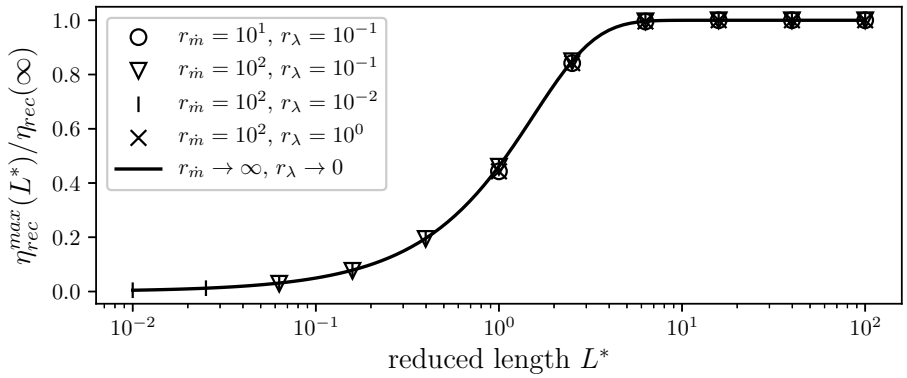

Figure 10.: Convergence towards the infinite porous medium case - universal curve in the conditions (37) and (63).

with solid conductivity, volume heat transfer coefficient and adiabatic temperature. Two dimensionless numbers denoted $r_{\dot{m}}$ and r_λ drive this phenomena and the present study is valid for $r_{\dot{m}} \gg 0.1$ and $r_{\dot{m}}/r_\lambda \gg 10$, which is the transcription of the scale-separation hypothesis.

The analysis is then extended to finite-length porous burners and including heat loss through radiation at the extremities of the porous. Numerical resolution of the problem showed the existence of two solutions near the extremities of the porous, the one upstream being stable and the other one being unstable. This feature has already been discussed in the literature but variations in the length of the porous burner showed a convergence of the heat recirculation for normalised lengths $L^* > 5$. A parametric investigation pointed out that this convergence is independent of the porous flame parameters and solely determined by L^*, which is of practical interest for the design of porous burners.

Disclosure statement

No potential conflict of interest was reported by the authors.

Funding

This project has received funding from the European Research Council under the European Union's Horizon 2020 research and innovation programme Grant Agreement 832248, SCIROCCO.

References

[1] J. Howell, M. Hall, and J. Ellzey, *Combustion of hydrocarbon fuels within porous inert media*, Progress in Energy and Combustion Science 22 (1996), pp. 121 – 145, Available at http://www.sciencedirect.com/science/article/pii/0360128596000019.

[2] M. Kamal and A. Mohamad, *Combustion in porous media*, Proceedings of the Institution of Mechanical Engineers, Part A: Journal of Power and Energy 220 (2006), pp. 487–508.

[3] M.A. Mujeebu, M.Z. Abdullah, A. Mohamad, and M.A. Bakar, *Trends in modeling of porous media combustion*, Progress in Energy and Combustion science 36 (2010), pp. 627–650.
[4] F. Weinberg, *Combustion temperatures: the future?*, Nature 233 (1971), pp. 239–241.
[5] N.S. Kaisare and D.G. Vlachos, *A review on microcombustion: Fundamentals, devices and applications*, Progress in Energy and Combustion Science 38 (2012), pp. 321–359.
[6] J.L. Ellzey, E.L. Belmont, and C.H. Smith, *Heat recirculating reactors: Fundamental research and applications*, Progress in Energy and Combustion Science 72 (2019), pp. 32–58.
[7] J. Kiefer, M. Weikl, T. Seeger, F. Von Issendorff, F. Beyrau, and A. Leipertz, *Non-intrusive gas-phase temperature measurements inside a porous burner using dual-pump cars*, Proceedings of the Combustion Institute 32 (2009), pp. 3123–3129.
[8] J. Dunnmon, S. Sobhani, M. Wu, R. Fahrig, and M. Ihme, *An investigation of internal flame structure in porous media combustion via x-ray computed tomography*, Proceedings of the Combustion Institute 36 (2017), pp. 4399–4408.
[9] T. Takeno and K. Sato, *An excess enthalpy flame theory*, Combustion Science and Technology 20 (1979), pp. 73–84.
[10] T. Takeno, K. Sato, and K. Hase, *A theoretical study on an excess enthalpy flame*, in *Symposium (International) on Combustion*, Vol. 18. Elsevier, 1981, pp. 465–472.
[11] Y. Yoshizawa, K. Sasaki, and R. Echigo, *Analytical study of the structure of radiation controlled flame*, International Journal of Heat and Mass Transfer 31 (1988), pp. 311–319.
[12] P.F. Hsu and R.D. Matthews, *The necessity of using detailed kinetics in models for premixed combustion within porous media*, Combustion and flame 93 (1993), pp. 457–466.
[13] P.F. Hsu, W.D. EVANS, and J.R. HOWELL, *Experimental and numerical study of premixed combustion within nonhomogeneous porous ceramics*, Combustion Science and Technology 90 (1993), pp. 149–172.
[14] A.J. Barra and J.L. Ellzey, *Heat recirculation and heat transfer in porous burners*, Combustion and Flame 137 (2004), pp. 230–241.
[15] N. Djordjevic, P. Habisreuther, and N. Zarzalis, *A numerical investigation of the flame stability in porous burners employing various ceramic sponge-like structures*, Chemical engineering science 66 (2011), pp. 682–688.
[16] S. Panigrahy, *Investigation on combustion in porous inert burners using gaseous and liquid fuels*, Ph.D. diss., Indian Institute of Technology Guwahati, 2018.
[17] J. Li, Q. Li, J. Shi, X. Liu, and Z. Guo, *Numerical study on heat recirculation in a porous micro-combustor*, Combustion and flame 171 (2016), pp. 152–161.
[18] S. Sathe, R. Peck, and T. Tong, *A numerical analysis of heat transfer and combustion in porous radiant burners*, International Journal of Heat and Mass Transfer 33 (1990), pp. 1331–1338.
[19] D. Diamantis, E. Mastorakos, and D. Goussis, *Simulations of premixed combustion in porous media*, Combustion Theory and Modelling 6 (2002), pp. 383–411.
[20] Z. Jia, Q. Ye, H. Wang, H. Li, and S. Shi, *Numerical simulation of a new porous medium burner with two sections and double decks*, Processes 6 (2018), p. 185.
[21] C. Bedoya, I. Dinkov, P. Habisreuther, N. Zarzalis, H. Bockhorn, and P. Parthasarathy, *Experimental study, 1d volume-averaged calculations and 3d direct pore level simulations of the flame stabilization in porous inert media at elevated pressure*, Combustion and Flame 162 (2015), pp. 3740–3754.
[22] I. Dinkov, P. Habisreuther, and H. Bockhorn, *Numerical prediction of burning velocity and flame thickness in a radial-flow porous burner*, in *Proceedings of the European Combustion Meeting*. 2013, pp. P5–78.
[23] B. Deshaies and G. Joulin, *Asymptotic study of an excess-enthalpy flame*, Combustion Science and Technology 22 (1980), pp. 281–285.
[24] J. Buckmaster and T. Takeno, *Blow-off and flashback of an excess enthalpy flame*, Combustion Science and Technology (1981).
[25] F. Escobedo and H.J. Viljoen, *Modeling of porous radiant burners with large extinction*

coefficients, The Canadian Journal of Chemical Engineering 72 (1994), pp. 805–814.
[26] L. Boshoff-Mostert and H.J. Viljoen, *Analysis of homogeneous combustion in monolithic structures*, Chemical engineering science 51 (1996), pp. 1107–1111.
[27] F.M. Pereira, A.A. Oliveira, and F.F. Fachini, *Asymptotic analysis of stationary adiabatic premixed flames in porous inert media*, Combustion and Flame 156 (2009), pp. 152 – 165, Available at http://www.sciencedirect.com/science/article/pii/S0010218008002496.
[28] F.M. PEREIRA, A.A.M. OLIVEIRA, and F.F. FACHINI, *Theoretical analysis of ultra-lean premixed flames in porous inert media*, Journal of Fluid Mechanics 657 (2010), p. 285–307.
[29] F.M. Pereira, A.A. Oliveira, and F.F. Fachini, *Maximum superadiabatic temperature for stabilized flames within porous inert media*, Combustion and flame 158 (2011), pp. 2283–2288.
[30] X. Fu, R. Viskanta, and J. Gore, *Combustion and heat transfer interaction in a pore-scale refractory tube burner*, Journal of thermophysics and heat transfer 12 (1998), pp. 164–171.
[31] R. Fursenko, S. Minaev, and V. Babkin, *Thermal interaction of two flame fronts propagating in channels with opposing gas flows*, Combustion, Explosion and Shock Waves 37 (2001), pp. 493–500.
[32] P.D. Ronney, *Analysis of non-adiabatic heat-recirculating combustors*, Combustion and Flame 135 (2003), pp. 421–439.
[33] Y. Ju and C. Choi, *An analysis of sub-limit flame dynamics using opposite propagating flames in mesoscale channels*, Combustion and Flame 133 (2003), pp. 483–493.
[34] Y. Ju and B. Xu, *Theoretical and experimental studies on mesoscale flame propagation and extinction*, Proceedings of the Combustion Institute 30 (2005), pp. 2445–2453.
[35] I. Schoegl and J.L. Ellzey, *Superadiabatic combustion in conducting tubes and heat exchangers of finite length*, Combustion and flame 151 (2007), pp. 142–159.
[36] D. Lee and K. Maruta, *Heat recirculation effects on flame propagation and flame structure in a mesoscale tube*, Combustion Theory and Modelling 16 (2012), pp. 507–536.
[37] A. Aldushin and S. Kasparyan, *Stability of stationary filtrational combustion waves*, Combustion, Explosion and Shock Waves 17 (1981), pp. 615–625.
[38] V.S. Babkin, *Filtrational combustion of gases. present state of affairs and prospects*, Pure and Applied Chemistry 65 (1993), pp. 335 – 344, Available at https://www.degruyter.com/view/journals/pac/65/2/article-p335.xml.
[39] S. Zhdanok, L.A. Kennedy, and G. Koester, *Superadiabatic combustion of methane air mixtures under filtration in a packed bed*, Combustion and Flame 100 (1995), pp. 221–231.
[40] V. Zamashchikov, *An investigation of gas combustion in a narrow tube*, Combustion science and technology 166 (2001), pp. 1–14.
[41] V. Bubnovich, S. Zhdanok, and K. Dobrego, *Analytical study of the combustion waves propagation under filtration of methane–air mixture in a packed bed*, International Journal of Heat and Mass Transfer 49 (2006), pp. 2578–2586.
[42] H. Yang, S. Minaev, E. Geynce, H. Nakamura, and K. Maruta, *Filtration combustion of methane in high-porosity micro-fibrous media*, Combustion science and technology 181 (2009), pp. 654–669.
[43] F.A. Williams, *Combustion theory*, CRC Press, 2018.
[44] A. MOHAMAD, *11 - combustion in porous media: Fundamentals and applications*, in *Transport Phenomena in Porous Media III*, D. Ingham and I. Pop, eds., Pergamon, Oxford, 2005, pp. 287 – 304, Available at http://www.sciencedirect.com/science/article/pii/B9780080444901500156.
[45] C.K. LAW, *Propagation, structure, and limit phenomena of laminar flames at elevated pressures*, Combustion Science and Technology 178 (2006), pp. 335–360, Available at https://doi.org/10.1080/00102200500290690.
[46] R.M. Corless, G.H. Gonnet, D.E. Hare, D.J. Jeffrey, and D.E. Knuth, *On the lambertw function*, Advances in Computational mathematics 5 (1996), pp. 329–359.
[47] D.G. Goodwin, R.L. Speth, H.K. Moffat, and B.W. Weber, *Cantera: An object-*

oriented software toolkit for chemical kinetics, thermodynamics, and transport processes, https://www.cantera.org (2018). Version 2.4.0.

Appendix A. Gas temperature continuity

In this appendix, we prove the equivalence of gas temperature continuity and energy conservation from reaction (27), provided the continuity of the solid heat flux (26) and consistent boundary conditions (15-16):

$$T_g(x = 0^-) = T_g(x = 0^+) \iff (15) + (16) + (26) + (27). \tag{A1}$$

We reason without dimensions. Equations (12) and (13) can be rearranged as follows, by substituting the term $\theta_s - \theta_g$:

$$r_\lambda \, \partial^2\theta_g + \partial^2\theta_s = r_{\dot{m}} \, \partial\theta_g. \tag{A2}$$

By integrating Equation (A2) from $-\infty$ to 0^- in zone 1 and 0^+ to $+\infty$ in zone 2 and taking into account the boundary conditions (15-16), we find respectively:

$$r_\lambda \, \partial\theta_g^1(x^* = 0^-) + \partial\theta_s^1(x^* = 0^-) = r_{\dot{m}} \, \theta_g^1(x^* = 0^-), \tag{A3}$$

$$r_\lambda \, \partial\theta_g^2(x^* = 0^+) + \partial\theta_s^2(x^* = 0^+) = r_{\dot{m}} \left[\theta_g^2(x^* = 0^+) - 1\right]. \tag{A4}$$

Subtracting Equation (A3) to Equation (A4) and using solid heat flux continuity (26) yields:

$$\partial\theta_g^1(x^* = 0^-) - \partial\theta_g^2(x^* = 0^+) = \frac{r_{\dot{m}}}{r_\lambda} + \frac{r_{\dot{m}}}{r_\lambda} \left[\theta_g^1(x^* = 0^-) - \theta_g^2(x^* = 0^+)\right]. \tag{A5}$$

When the gas temperature is continuous at the origin, Equation (A5) simplifies to:

$$\partial\theta_g^1(x^* = 0^-) = \frac{r_{\dot{m}}}{r_\lambda} + \partial\theta_g^2(x^* = 0^+), \tag{A6}$$

which is the dimensionless form of Equation (27). This proves the equivalence (A1). The gas temperature is continuous over the entire gas domain.

Appendix B. Maximum of gas temperature at $x = 0$

We now show that the gas temperature is maximal at the origin:

$$\theta_{max} = \theta_g^1(x^* = 0^-) = \theta_g^2(x^* = 0^+). \tag{34}$$

Since the gas temperature is continuous over the entire domain, it is sufficient to show its strict increase in zone 1 and its strict decrease in zone 2. Recalling the sign of each root of Equation (20):

$$\lambda_1 < 0 < \lambda_2 < \lambda_3, \tag{B1}$$

and looking at Equations (23-24), it is clear that if:

$$A_i(1-\lambda_i^2) > 0, \tag{B2}$$

then the variations meet the researched property. To move forward, it is necessary to resolve formally the system (31-33). This gives:

$$A_1 = \frac{-\lambda_2\lambda_3}{(\lambda_2-\lambda_1)(\lambda_3-\lambda_1)}, \tag{B3}$$

$$A_2 = \frac{-\lambda_1\lambda_3}{(\lambda_2-\lambda_1)(\lambda_3-\lambda_2)}, \tag{B4}$$

$$A_3 = \frac{+\lambda_1\lambda_2}{(\lambda_3-\lambda_1)(\lambda_3-\lambda_2)}. \tag{B5}$$

By using Equation (B1), it is clear that the denominators in Equations (B3-B5) are positive. Then, taking into account the signs in front of the numerators, the condition (B2) breaks down into:

$$\lambda_2\lambda_3(1-\lambda_1^2) < 0, \qquad \lambda_1\lambda_3(1-\lambda_2^2) < 0 \qquad \text{and} \qquad \lambda_1\lambda_2(1-\lambda_3^2) > 0. \tag{B6}$$

This requires studying the sign of:

$$\lambda_i\lambda_j(1-\lambda_k^2), \tag{B7}$$

for the circular permutations $i, j, k \in \{1, 2, 3\}$. For that, we make use of the relations between the roots and the coefficients of the polynomial of Equation (20):

$$\lambda_1+\lambda_2+\lambda_3 = \frac{r_{\dot{m}}}{r_\lambda}, \tag{B8}$$

$$\lambda_1\lambda_2+\lambda_2\lambda_3+\lambda_1\lambda_3 = -\frac{1+r_\lambda}{r_\lambda}, \tag{B9}$$

$$\lambda_1\lambda_2\lambda_3 = -\frac{r_{\dot{m}}}{r_\lambda}. \tag{B10}$$

Using Equation (B10), the term (B7) becomes:

$$\lambda_i\lambda_j - (\lambda_i\lambda_j\lambda_k)\lambda_k = \lambda_i\lambda_j + \lambda_k\frac{r_{\dot{m}}}{r_\lambda}. \tag{B11}$$

Then, by using Equation (B9), it becomes:

$$-\frac{1+r_\lambda}{r_\lambda} - \lambda_j\lambda_k - \lambda_i\lambda_k + \lambda_k\frac{r_{\dot{m}}}{r_\lambda} = -\frac{1+r_\lambda}{r_\lambda} - \left(\lambda_j+\lambda_i-\frac{r_{\dot{m}}}{r_\lambda}\right)\lambda_k. \tag{B12}$$

And then thanks to Equation (B8), we find a compact form for (B7):

$$-\frac{1+r_\lambda}{r_\lambda} + \lambda_k^2, \tag{B13}$$

so that (B6) is equivalent to:

$$-\frac{1+r_\lambda}{r_\lambda}+\lambda_1^2<0, \qquad -\frac{1+r_\lambda}{r_\lambda}+\lambda_2^2<0, \qquad \text{and} \qquad -\frac{1+r_\lambda}{r_\lambda}+\lambda_3^2>0. \tag{B14}$$

One way to prove (B14) is to use the continuity and monotony of the roots with regard to $r_{\dot{m}}$. The monotony can be seen by considering the form (C5) given in Appendix C. Keeping in mind the ordering $\lambda_1<0<\lambda_2<\lambda_3$, let us study the roots of (20) when $r_{\dot{m}}\to 0$ and $r_{\dot{m}}\to+\infty$. We find:

$$r_{\dot{m}}\to 0 \quad \Longrightarrow \quad \lambda_1\to-\frac{1+r_\lambda}{r_\lambda}, \quad \lambda_2\to 0 \quad \text{and} \quad \lambda_3\to\frac{1+r_\lambda}{r_\lambda}, \tag{B15}$$

$$r_{\dot{m}}\to+\infty \quad \Longrightarrow \quad \lambda_1\to-1, \quad \lambda_2\to 1 \quad \text{and} \quad \lambda_3\to+\infty. \tag{B16}$$

Since $(1+r_\lambda)/r_\lambda>1$, it is found that:

$$\lambda_1\in\left]-\frac{1+r_\lambda}{r_\lambda},-1\right[, \qquad \lambda_2\in\,]0,1[\qquad \text{and} \qquad \lambda_3\in\left]\frac{1+r_\lambda}{r_\lambda},+\infty\right[, \tag{B17}$$

what leads to (B14). This proves that the maximum temperature is reached at $x=0$.

Appendix C. Characteristic polynomial

In this appendix, the characteristic polynomial of Equation (20) is scrutinized. The general forms of its roots and their respective Taylor developments in the regime (37) are given. So as to simplify further calculations, the following notations are introduced:

$$\varepsilon=\frac{r_\lambda}{r_{\dot{m}}} \qquad \text{and} \qquad \chi=\frac{1+r_\lambda}{r_\lambda}>1. \tag{C1}$$

Equation (20) becomes:

$$\lambda^3-\varepsilon^{-1}\lambda^2-\chi\,\lambda+\varepsilon^{-1}=0. \tag{C2}$$

Following Cardano's general theory, the canonical variables are introduced:

$$p=-\left(\frac{1}{3\varepsilon^2}+\chi\right) \qquad \text{and} \qquad q=-\frac{1}{3\varepsilon}\left(\frac{2}{9\varepsilon^2}+\chi-3\right). \tag{C3}$$

The discriminant of Equation (C2) is:

$$\Delta=-(4p^3+9q^2)=\frac{4}{\varepsilon^4}+\frac{9(2\chi-1)}{\varepsilon^2}+4\chi^2>0, \tag{C4}$$

whose positivity comes from $\chi>1$. This confirms that Equation (20) has three real solutions $(\lambda_1,\lambda_2,\lambda_3)\in\mathbb{R}^3$. Using the relations (B8-B10), namely the negatitivy of their product and the positivity of their sum, it is deduced that their sign follows (B1).

The general solutions take the following form:

$$\lambda_k = \frac{1}{3\varepsilon} + 2\sqrt{\frac{-p}{3}}\cos\left[\frac{1}{3}\arccos\left(\frac{3q}{2p}\sqrt{\frac{3}{-p}}\right) + \frac{2k\pi}{3}\right] \qquad \text{for } k \in \{1,2,3\}. \tag{C5}$$

The regime (37) can be recast in terms of ε and χ as:

$$r_{\dot{m}}^{-1} = (\chi - 1)\varepsilon \ll 10 \qquad \text{and} \qquad \left(\frac{r_{\dot{m}}}{r_\lambda}\right)^{-1} = \varepsilon \ll 0.1, \tag{C6}$$

which means that a Taylor development in ε near the origin is conceivable. After some calculations, this gives:

$$\lambda_1 = -1 - \frac{(\chi-1)}{2}\varepsilon - \frac{(\chi-5)(\chi-1)}{8}\varepsilon^2 + O(\varepsilon^3), \tag{C7}$$

$$\lambda_2 = 1 - \frac{(\chi-1)}{2}\varepsilon + \frac{(\chi-5)(\chi-1)}{8}\varepsilon^2 + O(\varepsilon^3), \tag{C8}$$

$$\lambda_3 = \frac{1}{\varepsilon} + (\chi-1)\varepsilon + O(\varepsilon^3). \tag{C9}$$

It is worth noting that often, terms similar to $(\chi-1)\varepsilon$ appear in the expansions. This is the translation that roughly, the regime (37) corresponds to $r_{\dot{m}} \to +\infty$ for a fixed r_λ. These developments show that the approximated roots found in Section 2.4 are dominant-order approximations in ε. The roots λ_1 and λ_2 tend to be symmetric, of norm close to unity, while λ_3 has a propensity to be large.

Appendix D. Matrix for resolution of the finite porous

$$\underline{\underline{\mathbf{M}}} = \begin{bmatrix}
1 & 1 & 1 \\
0 & \lambda_1 & \lambda_2 \\
1 & 1-\lambda_1^2 & 1-\lambda_2^2 \\
0 & \lambda_1(1-\lambda_1^2) & \lambda_2(1-\lambda_2^2) \\
0 & \lambda_1 e^{-\lambda_1 x_p^*} & \lambda_2 e^{-\lambda_2 x_p^*} \\
0 & \epsilon\lambda_1(1-\lambda_1^2)e^{-\lambda_1 x_p^*} & \epsilon\lambda_2(1-\lambda_2^2)e^{-\lambda_2 x_p^*} \\
1 & (1-\lambda_1^2)e^{-\lambda_1 x_p^*} & (1-\lambda_2^2)e^{-\lambda_2 x_p^*} \\
0 & 0 & 0 \\
0 & 0 & 0
\end{bmatrix}$$

$$\begin{bmatrix}
1 & -1 & -1 \\
\lambda_3 & 0 & -\lambda_1 \\
1-\lambda_3^2 & -1 & -(1-\lambda_1^2) \\
\lambda_3(1-\lambda_3^2) & 0 & -\lambda_1(1-\lambda_1^2) \\
0 & 0 & \lambda_1(1-\lambda_1^2)e^{\lambda_1(L^*-x_p^*)} \\
\epsilon\lambda_3(1-\lambda_3^2)e^{-\lambda_3 x_p^*} & 0 & 0 \\
(1-\lambda_3^2)e^{-\lambda_3 x_p^*} & 0 & 0 \\
\lambda_3 e^{-\lambda_3 x_p^*} & 0 & 0 \\
0 & 0 & \lambda_1 e^{\lambda_1(L^*-x_p^*)}
\end{bmatrix}$$

$$\begin{bmatrix}
-1 & -e^{-\lambda_3(L^*-x_p^*)} & 0 \\
-\lambda_2 & -\lambda_3 e^{-\lambda_3(L^*-x_p^*)} & 0 \\
-(1-\lambda_2^2) & -(1-\lambda_3^2)e^{-\lambda_3(L^*-x_p^*)} & 0 \\
-\lambda_2(1-\lambda_2^2) & -\lambda_3(1-\lambda_3^2)e^{-\lambda_3(L^*-x_p^*)} & 0 \\
0 & 0 & 0 \\
0 & 0 & -r_{\dot{m}}/r_\lambda \\
0 & 0 & -1 \\
\lambda_2 e^{\lambda_2(L^*-x_p^*)} & \lambda_3 & 0 \\
\lambda_2(1-\lambda_2^2)e^{\lambda_2(L^*-x_p^*)} & \lambda_3(1-\lambda_3^2) & 0
\end{bmatrix} \quad \text{(D1)}$$